2D Materials

Fine structure of K-excitons in multilayers of transition metal dichalcogenides

To cite this article: A O Slobodeniuk *et al* 2019 *2D Mater.* **6** 025026

IOP Publishing 2D Mater. 6 (2019) 025026 https://doi.org/10.1088/2053-1583/ab0776

2D Materials

OPEN ACCESS

RECEIVED
5 January 2019

REVISED
20 January 2019

ACCEPTED FOR PUBLICATION
15 February 2019

PUBLISHED
28 February 2019

PAPER

Fine structure of K-excitons in multilayers of transition metal dichalcogenides

A O Slobodeniuk[1], Ł Bala[1,2], M Koperski[1,3,4], M R Molas[1,2], P Kossacki[2], K Nogajewski[1,2], M Bartos[1], K Watanabe[5], T Taniguchi[5], C Faugeras[1] and M Potemski[1,2]

[1] Laboratoire National des Champs Magnétiques Intenses, CNRS-UGA-UPS-INSA-EMFL, 25 avenue des Martyrs, 38042 Grenoble, France
[2] Faculty of Physics, Institute of Experimental Physics, University of Warsaw, ul. Pasteura 5, 02-093 Warszawa, Poland
[3] School of Physics and Astronomy, University of Manchester, Oxford Road, Manchester, M13 9PL, United Kingdom
[4] National Graphene Institute, University of Manchester, Oxford Road, Manchester, M13 9PL, United Kingdom
[5] National Institute for Materials Science, 1-1 Namiki, Tsukuba 305-0044, Japan

E-mail: artur.slobodeniuk@lncmi.cnrs.fr **and** marek.potemski@lncmi.cnrs.fr

Keywords: transition metal dichalcogenide multilayers, excitons, $\mathbf{k}\cdot\mathbf{p}$ method, reflectance measurements

Abstract

Reflectance and magneto-reflectance experiments together with theoretical modelling based on the $\mathbf{k}\cdot\mathbf{p}$ approach have been employed to study the evolution of direct bandgap excitons in MoS_2 layers with a thickness ranging from mono- to trilayer. We observe extra excitonic resonances in MoS_2 multilayers which emerge as a result of the hybridization of Bloch states of each sub-layer due to the interlayer coupling. The properties of such excitons in bi- and trilayers are classified by the symmetry of the corresponding crystals. The inter- and intralayer character of the reported excitonic resonances is fingerprinted with the magneto-optical measurements: excitonic g-factors of opposite sign and of different amplitude are revealed for these two types of resonances. The parameters describing the strength of the spin–orbit interaction are estimated for bi- and trilayer MoS_2.

1. Introduction

Scientific curiosity to uncover the properties of new materials and to demonstrate their possible novel functionalities drives research efforts focused on atomically-thin matter, and, in particular, on thin layers of semiconducting transition metal dichalcogenides (S-TMD) [1–4]. Intense works have been devoted to studies of S-TMD monolayers which appeared to be the two-dimensional semiconductors with a direct bandgap positioned at the $K^{\pm}$ points of their 1st hexagonal Brillouin zone (BZ) [5, 6]. New and rich possibilities of tuning the band structure, the strength of Coulomb interaction, and thus the optical properties, are opened when stacking S-TMD monolayers, forming multilayers and/or hetero-layers [7–12]. The properties of the archetypes of S-TMD stacks which are the thermodynamically stable 2H-stacked multilayers are to be well understood first.

In 2H stacks of N monolayers (NML), the electronic bands are known to be effectively modified, with N, in the range outside the $K^{\pm}$ points of the BZ [13–19]. This, in particular, implies the indirect bandgap in NMLs when $N > 1$, what strongly affects the emission spectra of these multilayers [20–24]. Instead, more subtle effects of the hybridization of electronic states around the direct bandgap which appears at $K^{\pm}$ points of the BZ in any NML are relevant for absorption-type processes [25, 26]. Understanding the absorption response of S-TMD multilayers might be of special importance for their potential applications in photo-sensing or photo-voltaic devices [27].

In this paper we present theoretical outlines (based on $\mathbf{k}\cdot\mathbf{p}$ approach [13, 22, 25, 26, 28]) and experimental data (results of reflectance and magneto-reflectance measurements), which, in a consistent manner, unveil the nature of direct bandgap ($K^{\pm}$ points) excitonic transitions in 2H-stacked S-TMDs multilayers. The geometry of the 2H stacking, wherein each subsequent layer is 180° rotated around the previous one, induces interaction and hybridization of the Bloch states in $K^{+}/K^{-}/K^{+}\ldots(K^{-}/K^{+}/K^{-}\ldots)$ points of the subsequent monolayers, which form the $K^{+}(K^{-})$ valleys of the multilayer. Such non-trivial interlayer coupling delocalizes the electron states in the out-of-plane direction, which leads to the formation of new type of excitons, associated with $K^{\pm}$ valleys in multilayers as well as in bulk crystals [22, 29, 30]. We classify such excitons, associate them with the symmetry of the crystal and describe their properties in a simple theoretical frame. Notably, the intra- or interlayer character of the excitonic transitions is fingerprinted with, correspondingly, negative or positive sign of the g-factor associated to these transitions.

Due to the different symmetries of the conduction and valence band orbitals, the hybridization of $K^{\pm}$-electronic states in NML occurs predominantly in the valence band and is more effective when the spin–orbit splitting Δ_v in the valence band is small. MoS_2, with the smallest Δ_v among all other S-TMDs, is the material of choice for such investigation. Our experimental results have largely profited of the significantly improved optical quality of MoS_2 layers when they are encapsulated in between layers of hexagonal boron nitride (hBN) [31–35]. We consider the bi- and trilayer systems as the simplest multilayer representatives with different spatial symmetry.

Matching theory and experiment, we estimate that in our multilayers of MoS_2: (i) the interlayer excitons are by $\sim$20 meV less bound than the intralayer excitons, in bilayer and likely in trilayer, (ii) in both bi- and trilayer, the spin–orbit splitting in the conduction band is of about 50 meV, that is larger than its counterpart in a monolayer [36], (iii) the two spin-orbit-split valence-band subbands are separated by 120 meV in bilayer, (iv) four spin-orbit-split subbands appear in the valence band of the trilayer; the two outer subbands are separated by 180 meV whereas the inner ones by 140 meV.

The paper is organized as follows. Section 2 introduces the theoretical description of the interlayer coupling and of optically active transitions in 2H stacked multilayers. In section 3, we present experimental data for excitonic resonances in bi- and trilayer of MoS_2. In section 4, we outline the properties of multilayers and the possible applications of such materials. In appendix A, the samples, instrumentation and experimental details are presented. Appendices B and C contain the derivation and discussion of the exciton g-factors in bi- and trilayer of MoS_2, respectively.

2. Theoretical description

We consider the optically active transitions at the $K^{\pm}$ points in 2H-stacked multilayers of S-TMD encapsulated in hBN. Our investigation is based on $\mathbf{k}\cdot\mathbf{p}$ approximation. We focus on the optical properties of such crystals at the K^{+} point for brevity [22]. The results for the K^{-} point can be obtained by analogy.

We briefly remind the basic properties of S-TMD *monolayers* which will be used in the subsequent description of multilayer structures. Namely, a single layer crystal is a direct band gap semiconductor. The maximum of the valence (VB) and minimum of the conduction (CB) bands are located at the $K^{\pm}$ points of the BZ. Due to the strong spin–orbit interaction, both bands are spin-split (from hundreds of meV in the VB, up to tens of meV in the CB). Hence, Bloch states in the corresponding points can be presented as a tensor product of spin and spinless states. The spinless valence $|\Psi_v\rangle$ and conduction $|\Psi_c\rangle$ band states at the K^{+} point are made predominantly from, correspondingly, $d_{x^2-y^2}+id_{xy}$ and d_{z^2} orbitals of transition metal atoms [37, 38]. Due to time-reversal symmetry (TRS) the analogous states at the K^{-} point are complex conjugated to the previous ones, i.e. they are made from $d_{x^2-y^2}-id_{xy}$ and d_{z^2} orbitals. The TRS also dictates that Bloch states with the same band index (c or v) but with opposite spins in different valleys have equal energies. The crystal spatial symmetry together with TRS define the optical properties of monolayers—only σ^{+} (σ^{-}) polarized light can be absorbed or emitted at the K^{+} (K^{-}) point. Since the VB and CB are split, there are two possible optical transitions (which conserve spin) at each K^{+} and K^{-} points—the lower-energy transition, T_A, and the higher-energy one, T_B. All the described features are depicted in figure 1 for the case of MoS_2 monolayer.

A *bilayer* crystal can be viewed as two monolayers separated by a distance $l\sim 6$ Å [39], and stacked in a way that the top layer is rotated with respect to the bottom one by 180°. We arrange them in $z=l/2$ and $z=-l/2$ planes, respectively (side view of the system is presented in figure 2). Then, the crystal possesses the centrosymmetry I with an inversion center in the $z=0$ plane (see two-headed red arrows in figure 2). This symmetry is preserved in our bilayer surrounded by rather thick hBN flakes[6]. Therefore, one can extend the $\mathbf{k}\cdot\mathbf{p}$ model proposed in [25, 26] also for this case.

Let us examine the Bloch states of the valence and conduction bands at the K^{+} point of a MoS_2 bilayer. We construct them from the Bloch states of the top and bottom layers considering them separately. Namely, we introduce the states $|\Psi_n^{(m)}\rangle\otimes|s\rangle$, where $m=1,2$ is a layer index (for bottom and top layers, respectively), $n=v,c$ is a band index (for VB and CB) and $s=\uparrow,\downarrow$ accounts for the spin degree of freedom. The bottom (first) layer states $|\Psi_v^{(1)}\rangle$ and $|\Psi_c^{(1)}\rangle$ are made predominantly from $d_{x^2-y^2}+id_{xy}$ and d_{z^2} orbitals of transition metal atoms respectively [37, 38]. They coincide with monolayer spinless states $|\Psi_v\rangle$ and $|\Psi_c\rangle$ mentioned before. The top (second) layer states $|\Psi_v^{(2)}\rangle$ and $|\Psi_c^{(2)}\rangle$ are made from $d_{x^2-y^2}-id_{xy}$ and d_{z^2} orbitals and coincide with spinless states at the K^{-} point of monolayer. The top and bottom states are connected

---

[6] It is worth noting that the distance between the layers in encapsulated S-TMD flakes can deviate from their non-encapsulated analogs, but the inversion (mirror symmetry) remains preserved in our bilayer (trilayer) structure. The AFM measurements of our samples indicate that the hBN-MoS_2 separation, $\delta=3.95$ Å, is the same in all three structures, whereas the MoS_2-MoS_2 interlayer distance, $l=5.4$ Å, identical for bi- and trilayer, is slightly smaller that in bulk MoS_2 (6.15 Å).

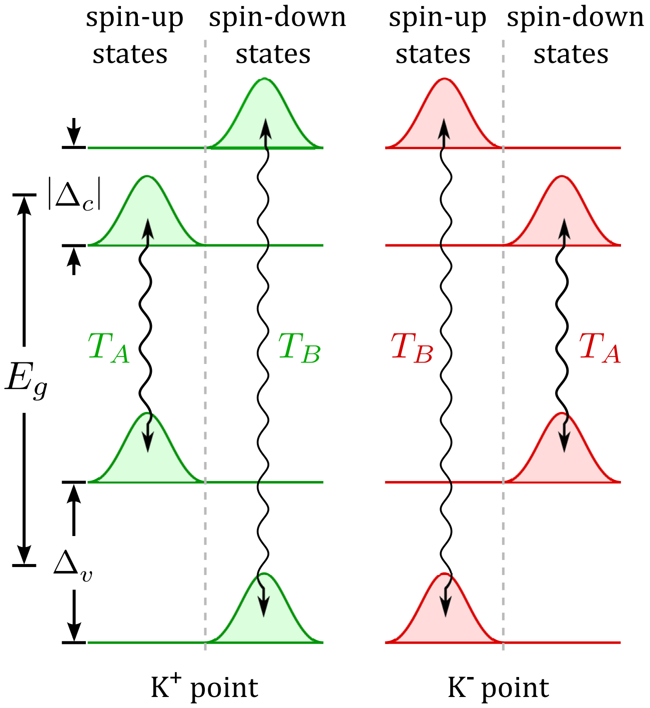

Figure 1. Sketch of band positions and optical transitions at the K$^+$ and K$^-$ points of the Brillouin zone in a monolayer of MoS$_2$. Bump structures represent the conduction and valence band states associated with optically active transitions, (T_A and T_B, shown with wave arrows), in σ^+ and σ^- configurations, coded in green and red, respectively.

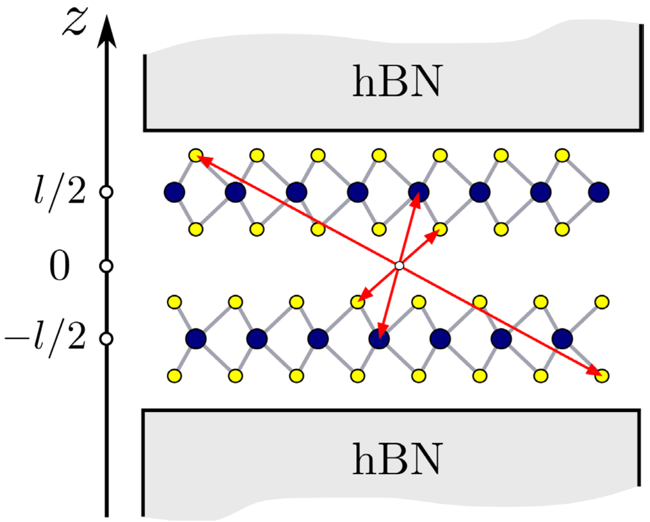

Figure 2. The bilayer S-TMD crystal embedded in between two thick hBN flakes, side view. Yellow and blue circles depict chalcogene and transition metal atoms, respectively. Red, two-headed arrows illustrate the inversion symmetry of the crystal.

by the relation $|\Psi_n^{(2)}\rangle = K_0 I |\Psi_n^{(1)}\rangle$, where K_0 and I are the complex conjugation and central inversion operators, respectively. Finally, we suppose the orthogonality of the basis states from different layers and bands $\langle\Psi_n^{(m)}|\Psi_{n'}^{(m')}\rangle = \delta_{nn'}\delta_{mm'}$.

The initial basis states in a given layer are affected by crystal field of the another layer and by the surrounding hBN medium. Such field, being considered as a perturbation in the $\mathbf{k}\cdot\mathbf{p}$ model, produces intra- and interlayer corrections to the bilayer Hamiltonian. The intralayer corrections renormalize the band gap E_g and spin-splittings Δ_c, Δ_v for the electron excitations in the considered layer. There is also a Rashba-like coupling between the VB (CB) basis states within the same layer. It is induced by the spin–orbit interaction. However, the strength of such coupling appears to be small and is neglected here [26]. Due to the symmetry of the crystal, the parameters of the other layer are similarly affected. The interlayer corrections link the states from different layers. The symmetry analysis of such terms demonstrates the existence of: (i) strong coupling between the VB basis states with the same spins,

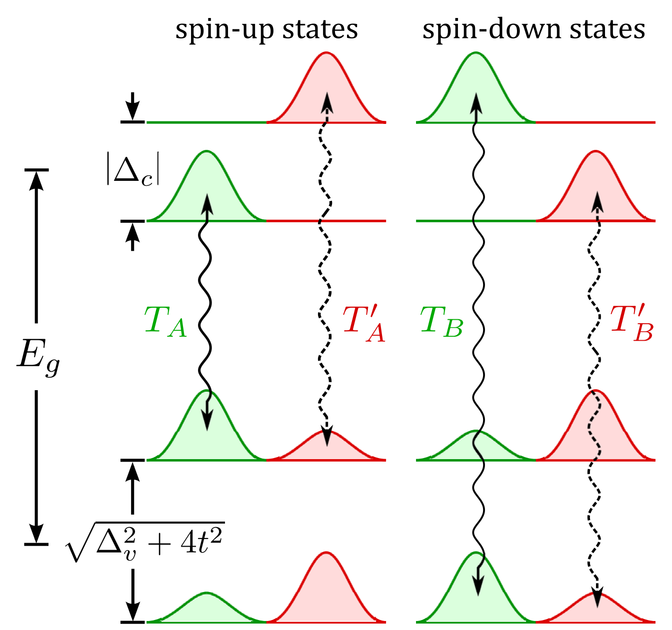

Figure 3. Sketch of the bands positions and optical transitions at the K$^+$ point of the BZ in a bilayer of MoS$_2$. Green and red bump structures represent the conduction and valence band states associated with optical transitions active in the σ^+ and σ^- polarizations, respectively. Solid (dashed) wavy arrows denote optical transitions T_A, T_B (T'_A, T'_B) due to the intralayer (interlayer) A and B excitons. $|\Delta_c|$ and $\sqrt{\Delta_v^2+4t^2}$ denote the splitting in the CB and the VB, respectively. E_g is the single particle band gap.

and (ii) the quasi-momentum dependent coupling between the CB basis states with the same spins. In our case, the spin-up and spin-down states of a bilayer are decoupled and can be considered separately.

As a result, the VB Hamiltonian, written in the $\{|\Psi_v^{(1)}\rangle \otimes |s\rangle, |\Psi_v^{(2)}\rangle \otimes |s\rangle\}$ basis, takes the form

$$H_{vs}^{(2)} = \begin{bmatrix} \sigma_s \frac{\Delta_v}{2} & t \\ t & -\sigma_s \frac{\Delta_v}{2} \end{bmatrix}, \qquad (1)$$

where $\sigma_s = +1(-1)$ for $s = \uparrow (\downarrow)$. The parameter $t \sim 40$–70 meV [25] defines the coupling between valence bands from different layers. The CB Hamiltonian, written in the basis $\{|\Psi_c^{(1)}\rangle \otimes |s\rangle, |\Psi_c^{(2)}\rangle \otimes |s\rangle\}$ is

$$H_{cs}^{(2)} = \begin{bmatrix} E_g + \sigma_s \frac{\Delta_c}{2} & uk_+ \\ uk_- & E_g - \sigma_s \frac{\Delta_c}{2} \end{bmatrix}, \qquad (2)$$

where $k_\pm = k_x \pm ik_y$ and E_g is the band gap of the bilayer. The parameter u defines the coupling between the conduction band states of the different layers. Its numerical value can be calculated from the microscopic model of S-TMD multilayers [26]. Both Hamiltonians are written up to $O(k^2)$.

The bilayer VB have energies $E_v^\pm = \pm\sqrt{\Delta_v^2/4 + t^2}$. The corresponding upper-energy eigenstates are

$$|\Phi_{v\uparrow}^+\rangle = \left[\cos\theta|\Psi_v^{(1)}\rangle + \sin\theta|\Psi_v^{(2)}\rangle\right] \otimes |\uparrow\rangle, \qquad (3a)$$

$$|\Phi_{v\downarrow}^+\rangle = \left[\sin\theta|\Psi_v^{(1)}\rangle + \cos\theta|\Psi_v^{(2)}\rangle\right] \otimes |\downarrow\rangle, \qquad (3b)$$

where we introduced $\cos(2\theta) = \Delta_v/\sqrt{\Delta_v^2 + 4t^2}$. The low-energy eigenstates $|\Phi_{v\uparrow}^-\rangle$ and $|\Phi_{v\downarrow}^-\rangle$ can be derived from those shown above by replacing $\cos\theta \to -\sin\theta, \sin\theta \to \cos\theta$. The new VB states are doubly degenerated with respect to spin.

The CB states do not interact with each other in K$^+$ valley (i.e. in the limit of $k_x, k_y \to 0$). Hence, in the leading order, they are not mixed and form doubly degenerated bands with energies $E_g \pm \Delta_c/2$. In the following we focus on a MoS$_2$ bilayer with $\Delta_c < 0$. For this case, the upper and lower energy CB states are $|\Psi_c^{(1)}\rangle \otimes |\downarrow\rangle, |\Psi_c^{(2)}\rangle \otimes |\uparrow\rangle$ and $|\Psi_c^{(1)}\rangle \otimes |\uparrow\rangle, |\Psi_c^{(2)}\rangle \otimes |\downarrow\rangle$, respectively.

All new energy states of a bilayer system are depicted graphically in figure 3. We divide them into spin-up (left panel in figure 3) and spin-down (right panel) subsets. The single and doubled bumps in the figure represent the new CB and VB states. The size of the bump reflects a probability to observe the new composite quasiparticle in the bottom (green part) or the top (red part) layers. The effective hybridization of valence band states implies that the transitions from any valence band state into both $|\Psi_c^{(1)}\rangle$ and $|\Psi_c^{(2)}\rangle$ states are now possible, in σ^+ and σ^- circularly polarized light, respectively. As a consequence, the system demonstrates four types of optically active transitions: two intralayer and two interlayer ones. One representative family of T_A, T'_A and T_B, T'_B transitions associated, correspondingly, with the spin-up and spin-down bands, are depicted in figure 3.

The two intralayer transitions of our bilayer

$$T_A: \begin{cases} |\Phi_{v\uparrow}^+\rangle \to |\Psi_c^{(1)}\rangle \otimes |\uparrow\rangle, \\ |\Phi_{v\downarrow}^+\rangle \to |\Psi_c^{(2)}\rangle \otimes |\downarrow\rangle; \end{cases} \qquad (4)$$

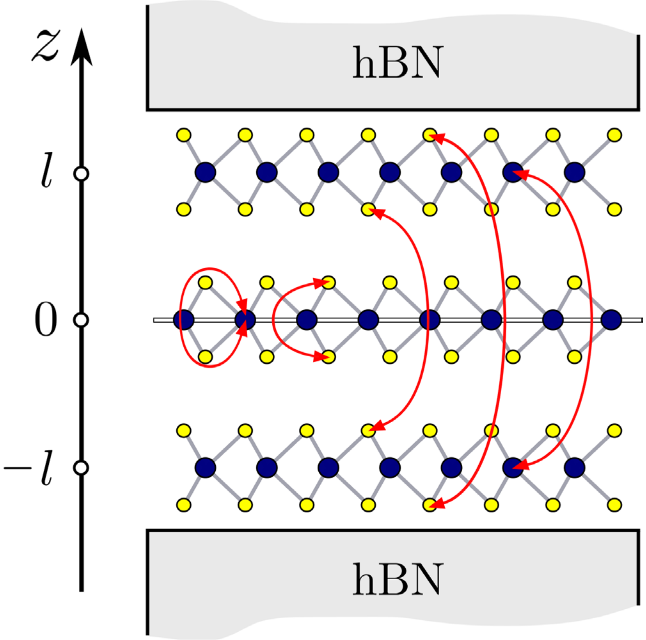

Figure 4. The trilayer S-TMD crystal embedded in between two thick hBN flakes, side view. Yellow and blue circles depict chalcogene and transition metal atoms, respectively. The thin white rectangular represents the mirror symmetry plane $z = 0$ of the trilayer. The tips of red curvy double-headed arrows couple the atoms, which coordinates transform into each other under mirror symmetry transformation.

$$T_B : \begin{cases} |\Phi^-_{v\uparrow}\rangle \to |\Psi^{(2)}_c\rangle \otimes |\uparrow\rangle, \\ |\Phi^-_{v\downarrow}\rangle \to |\Psi^{(1)}_c\rangle \otimes |\downarrow\rangle; \end{cases} \tag{5}$$

have the same intensity $I = I_0 \cos^2\theta$, where I_0 is the intensity of the corresponding transition in a monolayer.

The two interlayer transitions

$$T'_A : \begin{cases} |\Phi^+_{v\uparrow}\rangle \to |\Psi^{(2)}_c\rangle \otimes |\uparrow\rangle, \\ |\Phi^+_{v\downarrow}\rangle \to |\Psi^{(1)}_c\rangle \otimes |\downarrow\rangle; \end{cases} \tag{6}$$

$$T'_B : \begin{cases} |\Phi^-_{v\uparrow}\rangle \to |\Psi^{(1)}_c\rangle \otimes |\uparrow\rangle, \\ |\Phi^-_{v\downarrow}\rangle \to |\Psi^{(2)}_c\rangle \otimes |\downarrow\rangle; \end{cases} \tag{7}$$

are characterized by the intensity $I' = I_0 \sin^2\theta$. It is worth mentioning that the intra- and inter-layer transitions are active in opposite circular polarization at a given K point and thus the excitons associated with these two type of distinct transitions should display the opposite signs of g-factors (see appendix B).

The *trilayer* crystal can be seen as three monolayers separated by distance l, with the middle layer being rotated by 180° with respect to the external ones (side view of the system is shown in figure 4).

Similarly to the case of bilayer, we focus on the properties of quasiparticles at the K^+ point. The basis states of a trilayer are $\{|\Psi^{(1)}_n\rangle \otimes |s\rangle, |\Psi^{(2)}_n\rangle \otimes |s\rangle, |\Psi^{(3)}_n\rangle \otimes |s\rangle\}$. They belong to $z = -l$, $z = 0$ and $z = l$ layers, respectively. The trilayer crystal has mirror symmetry σ_h, with the mirror plane $z = 0$. It determines the symmetry relations $|\Psi^{(3)}_n\rangle = \sigma_h|\Psi^{(1)}_n\rangle, |\Psi^{(2)}_n\rangle = \sigma_h|\Psi^{(2)}_n\rangle$. The properties of $|\Psi^{(1)}_n\rangle$ and $|\Psi^{(2)}_n\rangle$ states are the same as in bilayer. The properties of $|\Psi^{(3)}_n\rangle$ states coincide with $|\Psi^{(1)}_n\rangle$ according to the crystal symmetry. Hence, at the K^+ point, the 1st and 3d layers absorb only σ^+ polarized light, while the 2nd one is active in σ^- polarization.

We derive the effective $\mathbf{k}\cdot\mathbf{p}$ Hamiltonian by considering the system within several approximations: (i) the intralayer crystal field corrections are equal for each layers, i.e. electronic bands in each layers are characterized by the same band-gap E_g and spin-splitting Δ_v, Δ_c parameters, the magnitudes of which, however, can deviate from their bilayer analogs[7]; (ii) we neglect the coupling between the states of the top and bottom layers. In this approach, like in the case of bilayer, the spin-up and spin-down states of a trilayer are decoupled. The Hamiltonian for the VB states, written in the basis $\{|\Psi^{(1)}_v\rangle \otimes |s\rangle, |\Psi^{(2)}_v\rangle \otimes |s\rangle, |\Psi^{(3)}_v\rangle \otimes |s\rangle\}$, is

$$H^{(3)}_{vs} = \begin{bmatrix} \sigma_s\frac{\Delta_v}{2} & t & 0 \\ t & -\sigma_s\frac{\Delta_v}{2} & t \\ 0 & t & \sigma_s\frac{\Delta_v}{2} \end{bmatrix}. \tag{8}$$

---

[7] The middle and outer MoS_2 layers forming the trilayer crystal are characterized by different close surroundings. Thus, strictly speaking, the middle layer can have a different band-gap and spin-splittings in comparison to their counterparts in the top/bottom layer's bands. This can be included in the trilayer Hamiltonian but does not change our main conclusion about the existence of odd and even states, mentioned later. Therefore, we set all the diagonal parameters equal to each other in order to avoid the excessive complication of the model.

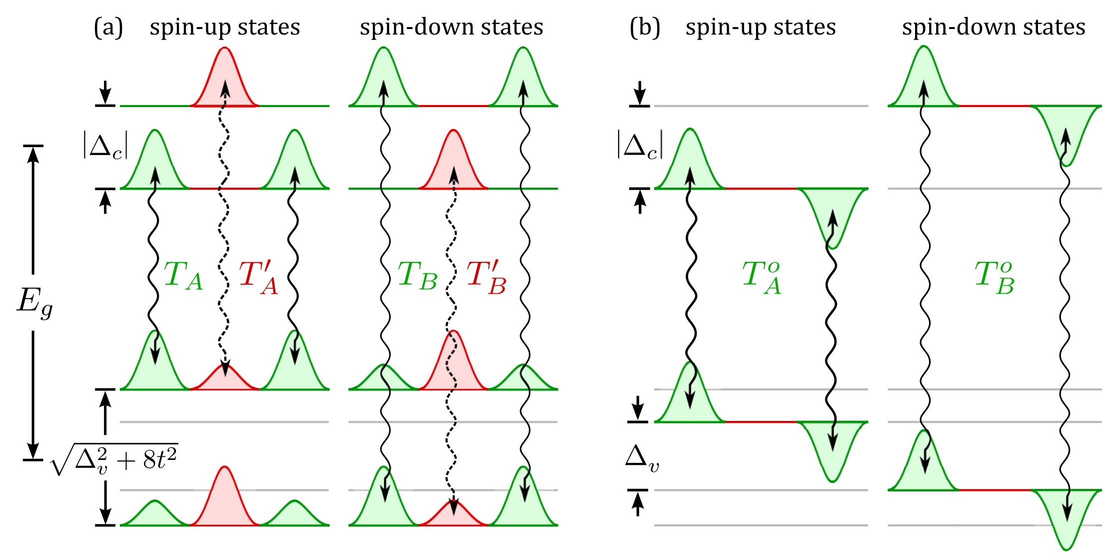

Figure 5. Sketch of bands positions and optical transitions between (a) even and (b) odd states at the K^+ point of the BZ in a trilayer of MoS_2. Green and red bump structures represent the conduction and valence band states associated with transitions, active in the σ^+ and σ^- polarizations, respectively. Solid (dashed) wavy arrows denote optical transitions due to the intralayer (interlayer) A and B excitons. $|\Delta_c|$ and $\sqrt{\Delta_v^2+8t^2}$ (Δ_v) denote the splitting in the CB and even (odd) states of the VB, respectively. E_g is the single particle band gap.

The Hamiltonian for conduction bands, written in the basis $\{|\Psi_c^{(1)}\rangle\otimes|s\rangle, |\Psi_c^{(2)}\rangle\otimes|s\rangle, |\Psi_c^{(3)}\rangle\otimes|s\rangle\}$, reads

$$H_{cs}^{(3)} = \begin{bmatrix} E_g+\sigma_s\frac{\Delta_c}{2} & uk_+ & 0 \\ uk_- & E_g-\sigma_s\frac{\Delta_c}{2} & uk_- \\ 0 & uk_+ & E_g+\sigma_s\frac{\Delta_c}{2} \end{bmatrix}. \tag{9}$$

The system possesses a mirror symmetry. Hence, it is convenient to introduce new basis states which are even $|\Upsilon_n^{(1)}\rangle = \frac{1}{\sqrt{2}}[|\Psi_n^{(1)}\rangle + |\Psi_n^{(3)}\rangle]$, $|\Upsilon_n^{(2)}\rangle = |\Psi_n^{(2)}\rangle$ and odd $|\Upsilon_n^{(3)}\rangle = \frac{1}{\sqrt{2}}[|\Psi_n^{(1)}\rangle - |\Psi_n^{(3)}\rangle]$ under the σ_h transformation. The trilayer Hamiltonians have a block-diagonal form in the basis $\{|\Upsilon_n^{(1)}\rangle\otimes|s\rangle, |\Upsilon_n^{(2)}\rangle\otimes|s\rangle, |\Upsilon_n^{(3)}\rangle\otimes|s\rangle\}$

$$\mathcal{H}_{vs}^{(3)} = \begin{bmatrix} \sigma_s\frac{\Delta_v}{2} & \sqrt{2}t & 0 \\ \sqrt{2}t & -\sigma_s\frac{\Delta_v}{2} & 0 \\ 0 & 0 & \sigma_s\frac{\Delta_v}{2} \end{bmatrix}, \tag{10}$$

$$\mathcal{H}_{cs}^{(3)} = \begin{bmatrix} E_g+\sigma_s\frac{\Delta_c}{2} & \sqrt{2}uk_+ & 0 \\ \sqrt{2}uk_- & E_g-\sigma_s\frac{\Delta_c}{2} & 0 \\ 0 & 0 & E_g+\sigma_s\frac{\Delta_c}{2} \end{bmatrix}. \tag{11}$$

The 2×2 blocks have the same structure as the one of bilayer's Hamiltonians. Therefore, all the properties of the even states can be obtained from the results of a bilayer by replacing $t\to\sqrt{2}t, u\to\sqrt{2}u$. Consequently, there are doubly degenerated valence and conduction bands which define the intense T_A and T_B and weak T'_A and T'_B optical transitions with the characteristic σ^+ and σ^- polarization rules as depicted by, correspondingly, wavy-solid and dashed double-headed arrows in figure 5(a).

The 1×1 block has the structure of monolayer Hamiltonian. Hence, only T^o_A and T^o_B transitions between odd states of trilayer do appear. They are active in the same polarization as T_A and T_B transitions of monolayer and are represented by wavy solid double-headed arrows in figure 5(b).

To this end, the trilayer is expected to display two types of 'even' intralayer excitons: T_A and T_B, and two types of 'odd' intralayer excitons: T^o_A and T^o_B. All of them are active in σ^+ polarization at the K^+ point and have g-factors of the same sign. Instead,the interlayer 'even' excitons, T'_A and T'_B, are active in σ^- polarization at the K^+ point and have g-factors of opposite sign to that of intralayer excitons. The detailed description of g-factors of trilayers is presented in appendix C.

Our theoretical description predicts the number of exciton resonances and their polarization properties to be observed in experiments. However, the relative position of T_A and T^o_A excitons remains an open question. Indeed, both resonances are active in the same polarization and have similar g-factors, which can make them impossible to be identified experimentally. The analysis of the interference effects together with the consideration of the Coulomb interaction between the new quasiparticles may answer this question, but such analysis is, beyond the scope of the present work.

A summary of our theoretical predictions, i.e. the expected evolution of the pattern of optically active transitions in (1L) mono-, (2L) bi- and (3L) trilayer MoS_2 crystals is illustrated in figure 6.

3. Absorption resonances in MoS_2 multilayers

We have experimentally investigated a set of van der Waals heterostructures with optically active parts consisting of MoS_2 mono-, bi- and trilayer. The structures were prepared on ultraflat unoxidized

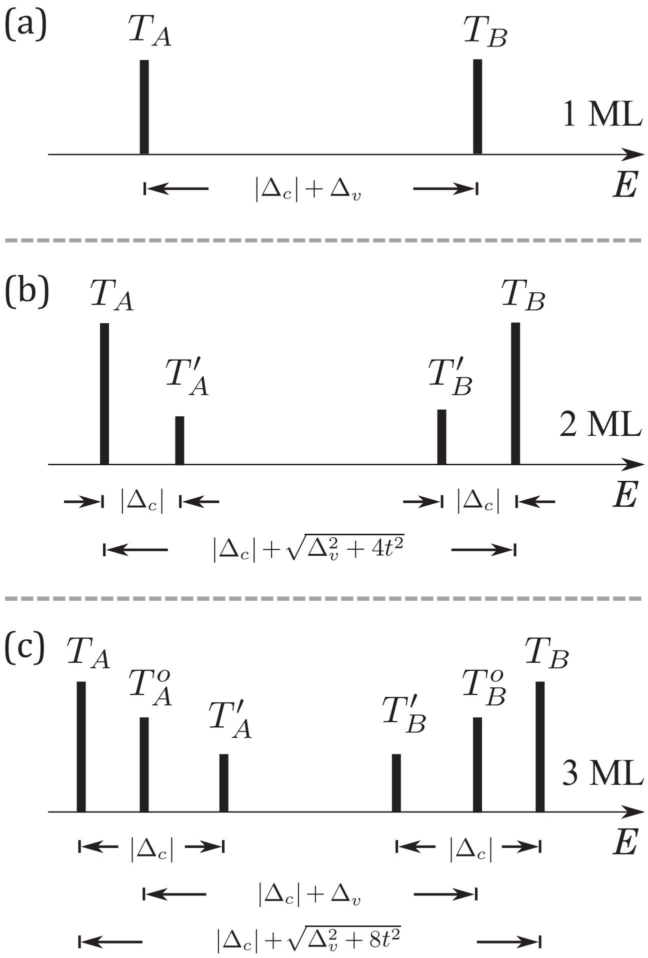

Figure 6. Sketch of optical transitions in (a) mono-, (b) bi- and (c) trilayer MoS_2 crystals. The position and size of black thick segments represent the energies and intensities of the corresponding transitions. The values of parameters Δ_c and Δ_v for bilayer and trilayer can deviate from their counterparts in monolayer analogs.

silicon substrates by combination of exfoliation and dry transfer techniques [40]. In order to achieve the highest possible quality of our samples, as well as to preserve the characteristic inverse and mirror symmetries of, respectively, 2H-stacked bi- and trilayer, the microcleaved MoS_2 flakes were sandwiched between two hBN flakes exfoliated from high-quality bulk crystals grown under high-pressure conditions [41]. Further information on the preparation of samples and their characterization is provided in appendix A.

Experiments consisted of measurements of the reflectance contrast (RC) spectrum, which is defined as

$$\mathrm{RC}(E) = \frac{R(E) - R_0(E)}{R(E) + R_0(E)} \times 100\%, \qquad (12)$$

where $R(E)$ is the reflectance spectrum when the light is focused on the MoS_2 flake and $R_0(E)$ is the reflectance from the region outside the flake. Two different micro-optical setups have been used: one setup for measurements in the absence of magnetic fields and the second one for measurements in magnetic fields supported by either a 14 T superconducting magnet or a 29 T resistive magnet. A spatial resolution of about 1 μm (light spot diameter) is characteristic of our free-beam-optics setup used for experiments at zero magnetic field. Instead, the fiber-optics-based arrangement applied for experiments in magnetic fields provides a poorer spatial resolution, of about 10 μm. A spectral resolution of 0.32 nm has been assured for both setups. A combination of a quarter wave plate and a polarizer are used to analyse the circular polarization of signals. The measurements are performed with a fixed circular polarization, whereas reversing the direction of magnetic field yields the information corresponding to the other polarization component due to TRS [30, 42]. More on experimental details can be found in appendix A.

The collection of low temperature (∼5 K) RC spectra using our $B = 0$ setup, measured in the spectral range of the optical gap (onset of strong absorption) of the MoS_2 layers is presented in figure 7.

The observed, more or less pronounced resonances, show a dispersive spectral shape and correspond to typically, strongly bound direct bandgap excitons in S-TMD layers. Although our theoretical considerations neglect the effects of Coulomb binding and account only for interband transitions, a resemblance between the measured spectral evolution pre-

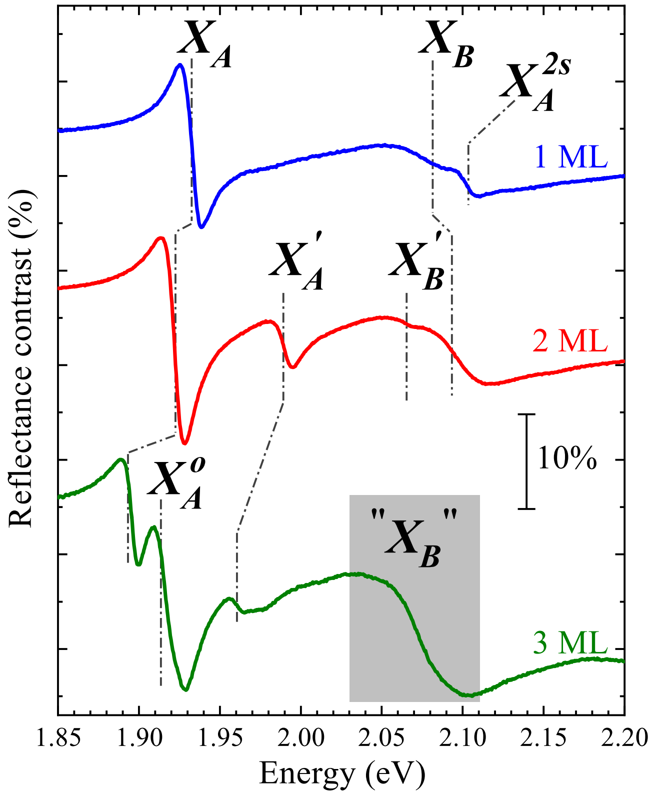

Figure 7. Reflectance contrast spectra of mono- (1L), bi- (2L) and trilayer (3L) MoS_2 crystals encapsulated in hBN measured at temperature 5 K. The spectra are vertically shifted for clarity.

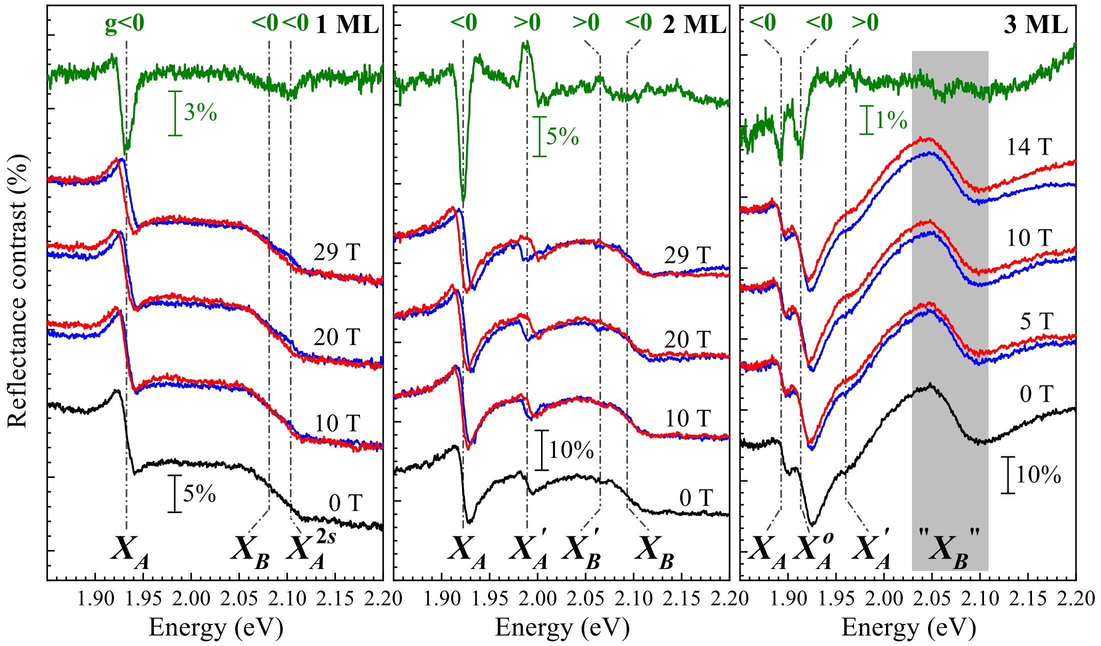

Figure 8. Helicity-resolved RC spectra (blue and red curves) of MoS_2 layers encapsulated in hBN for selected values of magnetic field, the corresponding zero-field RC spectrum (black curve), and differential spectra $\mathrm{RC}(\sigma^+, B = 29\ \mathrm{T}) - \mathrm{RC}(\sigma^+, B = -29\ \mathrm{T})$ (top panels), measured at temperature 4.2 K. The red and blue curves correspond to σ^+ polarization of reflected light in B and $-B$ configurations of magnetic field (applied perpendicularly to the layers plane), respectively. For differential spectra, deeps indicate a negative g-factor, while peaks indicate a positive g-factor of excitonic transitions. Vertical black and green bars define the scale for zero field RC and differential spectra, respectively. The spectra are vertically shifted for clarity.

sented in figure 7 and the theoretically concluded one in figure 6 can be recognized.

In the following we assume that each interband transition T_X is associated with the corresponding excitonic resonance X and we proceed with the assignment of the resonances observed in the experiment. We suppose that the resonating excitons are shifted in energy, by their binding energies, with respect to the associated

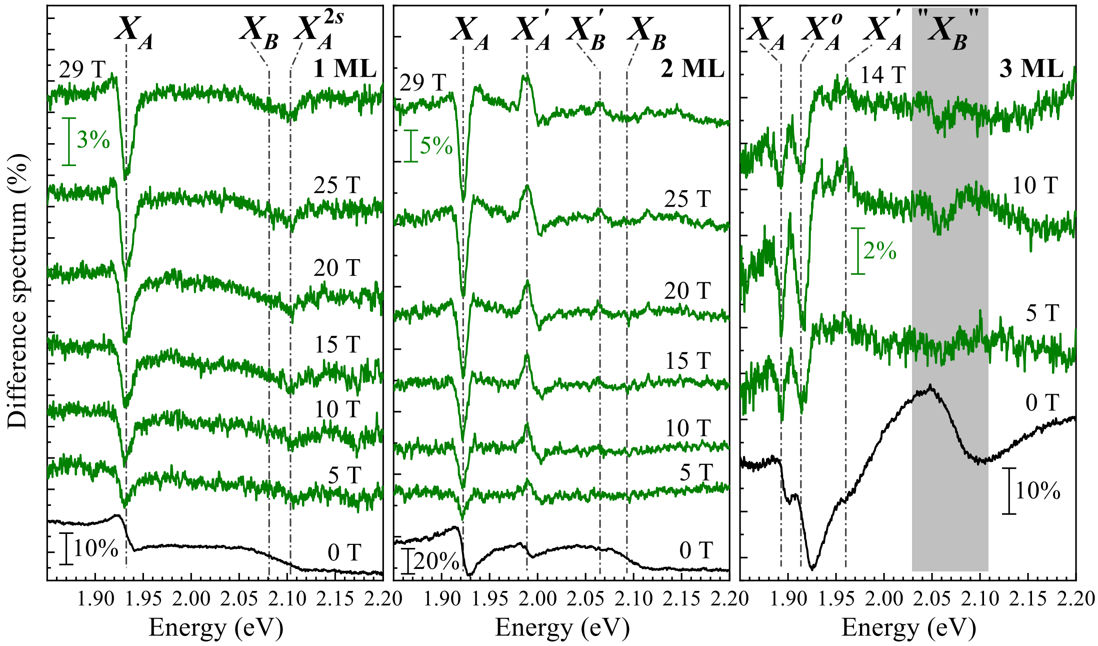

Figure 9. Zero-field RC spectra (black curve) and the differential spectra RC(σ^+, B) − RC($\sigma^+, -B$) at selected values of magnetic field B for 1 ML (left panel), 2 ML (middle panel) and 3 ML (right panel). Deeps in the difference spectra indicate a negative g-factor, while peaks indicate a positive g-factor of excitonic transitions. Vertical black and green bars define the scale for zero-filed RC and differential spectra, respectively. The spectra are vertically shifted for clarity.

interband transitions: $E(X) = E(T_X) - E_b(X)$. Binding energies might be, however, different for different excitons and this fact must be taken into account when comparing the energy position of X-resonances and T_X-transitions. Important for the assignment of the observed resonances are the results of the polarization resolved measurements carried out in magnetic fields (see figures 8 and 9).

As discussed above, we expect that our multilayers host two different types of intra- and interlayer excitons, each of them being distinguishable by their different polarization properties (g-factors of opposite sign and various magnitudes). At this point we must admit that all subtle spectral features which are well visible in the RC spectra measured at $B = 0$ with high spatial resolution are somewhat less pronounced in the magneto-optical measurements which imply a worse spatial resolution. A certain degree of sample inhomogeneity is an obvious cause of this drawback. In consequence, in the case of weak and/or broad resonances the information about their g-factors is not easily extractable from the raw magneto-RC data. This information becomes more apparent if we inspect the RC-polarization spectra. These spectra have been constructed as a difference between the RC-spectra measured at the same strength but for two opposite direction of the magnetic field (that mimic, due to the time reversal symmetry, the spectra corresponding to σ^+ and σ^- circular polarization of the reflected light). As can be deduced from the data shown in figures 8 and 9, the apparent dips in our differential RC polarization spectra correspond to excitonic resonances with negative g-factors whereas the characteristic upswings mark resonances with positive g-factors.

The very first classification of the observed resonances takes into account a relatively large spin–orbit splitting in the MoS_2 valence band, rising two groups of excitons associated with well-separated upper (A-excitons) and lower (B-excitons) valence band subbands. The 1 ML spectrum shown in figure 7, resembles that previously reported for a high quality 1 ML MoS_2 encapsulated in hBN [35]. It depicts three resonances: one well-separated resonance due to ground state A-exciton (X_A), and two other superimposed resonances, due to B-exciton (X_B) and the first excited ($2s$) state of A-exciton (X_A^{2s}). X_A and X_B resonances are associated with T_A and T_B transitions sketched in figure 1; the excited excitonic states are beyond the frame of our single particle theoretical approach. As expected, the X_A, X_B and X_A^{2s} excitonic resonances display similar polarization properties in the magneto-optical experiments (see top curve in the left panel of figure 8). We estimate $g_{X_A} \approx -4$ in agreement with previous reports [43–45]; the accurate estimation of the amplitudes of g_{X_B} and $g_{X_A^{2s}}$ is more cumbersome though both these values are also negative.

The RC spectrum of the 2 ML (see middle curve of figure 7) shows four resonances [29] which, in reference to our theoretical expectations (see figures 3 and 6), are assigned to the pair of intra- (X_A) and interlayer (X_A') A-excitons, and to the analogous pair of intra- (X_B) and interlayer (X_B') B-excitons. We use the signs and magnitudes of the exciton g-factors as fingerprints of the intra- and interlayer nature of the

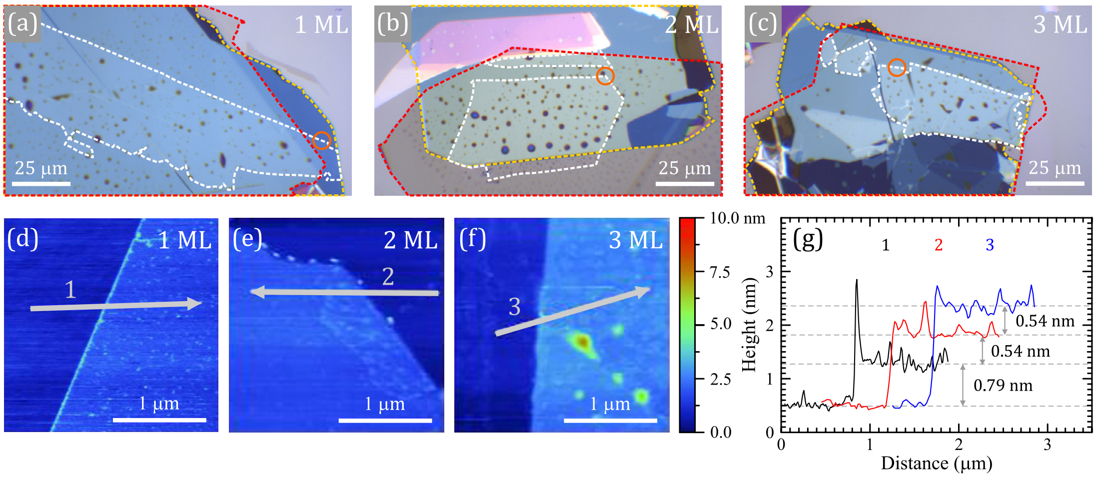

Figure A1. Upper row: optical microscope images of hBN/MoS_2/hBN heterostructures comprising (a) mono-, (b) bi- and (c) trilayer MoS_2 flakes (outlined in white) sandwiched between two hBN flakes—a 60–70 nm thick flake from the bottom (outlined in yellow) and 10–15 nm thick flake from the top (outlined in red). The spots of brown-to-blue colour visible in all images are bubbles of air and/or water vapour trapped between either the MoS_2 and the top hBN flake or the two hBN flakes. Lower row: (d)–(f) false colour atomic force microscope images taken at respective locations marked in (a)–(c) with orange circles. The grey arrows represent the line profiles drawn in panel (g) and labelled with the same numbers as in images (d)–(f).

X_A- and X'_A-excitons respectively [30]. Namely, we conclude that $g_{X_A} \approx -4$, while $g_{X'_A} \approx 8$. Again, the exact values for the *g*-factor amplitudes of *B*-excitons are hard to be precisely estimated. Nonetheless it is rather clear that g_{X_B} is negative and $g_{X'_B}$ is positive (see top curve in the middle panel of figure 8). Whereas our theoretical model meets the experimental data at the qualitative level, the energy ladder of the observed resonances requests further comments. Characteristic for the theoretical modelling is the fact that the energy distance, $\Delta(T'_A, T_A)$, between the T'_A and T_A transitions is the same as the energy separation, $\Delta(T_B, T'_B)$ between the T_B and T'_B transitions, both differences being determined by the amplitude Δ_c of the spin orbit splitting in the conduction band of the 2 ML: $\Delta(T'_A, T_A) = \Delta(T_B, T'_B) = |\Delta_c|$. This property is not seen in the experiment: we estimate that $\Delta(X'_A, X_A) \simeq 70$ meV, whereas $\Delta(X_B, X'_B) \simeq 30$ meV. The inconsistency between theory and experiment is likely due to the different binding energies of excitons associated with different interband transitions: $E(X) = E(T_X) - E_b(X)$. In the first approximation we assume that the binding energies of our inter- and intralayer excitons are indeed different but that the excitons within each pair of indirect and direct resonances are the same: $E_b(intra) = E_b(X_A) = E_b(X_B) \neq E_b(X'_A) = E_b(X'_B) = E_b(inter)$. Then, comparing the theoretical prediction with the experimental data one obtains that $|\Delta_c| = \Delta(T'_A, T_A) = \Delta(T_B, T'_B) = [\Delta(X'_A, X_A) + \Delta(X_B, X'_B)]/2 \simeq 50$ meV and that $E_b(intra) = E_b(inter) + 20$ meV. Larger binding energies of intralayer excitons with respect to those of interlayer excitons are logically expected since Coulomb attraction should be indeed stronger/weaker when the electron and hole charges are localized in the same or in the neighboring layers, as for the case of intra- or interlayer excitons, respectively. At first sight, the estimated amplitude of the spin orbit splitting in the conduction band of the MoS_2 bilayer appears to be surprisingly large. In the case of 1L MoS_2, the commonly accepted results of DFT calculations predict Δ_c in the range of few meV, though recent experimental works point out towards much higher values of about 15 meV [36]. According to our theoretical approach, the spin orbit interaction is sensitive to interlayer coupling and it is also affected by the interaction with the surrounding material (hBN). Thus the amplitudes of the Δ_c as well as Δ_v parameters are expected to evolve with the numbers of the stacked MoS_2 layers. Keeping our assumption about equal binding energies for X_A and X_B excitons we note that the expected energy separation between these excitonic resonance is given by $|\Delta_c| + \sqrt{\Delta_v^2 + 4t^2}$ (see figures 3 and 6), to be compared to the value of 170 meV estimated from the experiment. With the theoretically estimated value of $t \simeq 40$ meV [25] and the derived above $|\Delta_c| \simeq 50$ meV we find $\Delta_v \simeq 90$ meV. Visibly, however, the 'effective' spin orbit splitting in the valence band of the MoS_2 bilayer is larger, as given by $\sqrt{\Delta_v^2 + 4t^2} \simeq 120$ meV (see figure 3).

Focusing now on the trilayer spectrum (see bottom panel of figure 7) we observe a characteristic triplet of *A*-exciton resonances, which is in accordance with our theoretical expectations (see figure 6(c)). As expected, two strong X_A and X_A^o resonances are characterized by negative *g*-factors whereas the *g*-factor of the interlayer X'_A exciton is pretty much positive (see top curve in the right panel of figure 8). The theoretically anticipated triplet structure of the ″X''_B-exciton is not resolved in the experiment but likely hidden within the observed broad spectrum of the *B*-exciton. Even with unresolved fine structure of the *B*-exciton for our trilayer MoS_2, a rough estimation of Δ_c and Δ_v parameters can be done. Expecting that the energy separation between X'_A and X_A is $\Delta(X'_A, X_A) = |\Delta_c| + E_b(X_A) - E_b(X'_A)$ and reading $\Delta(X'_A, X_A) \simeq 70$ meV from the experiment we conclude that $|\Delta_c| \simeq 50$ meV if the difference between binding energies of the intralayer X_A and interlayer X'_A excitons is $E_b(X_A) - E_b(X'_A) \simeq 20$ meV, i.e. the same as we found for intra- and interlayer excitons in 2 ML MoS_2. On the other hand, supposing that binding energies of two X_A and X^o_A intralayer excitons are the same we expect that they are separated in energy by $\Delta(X^o_A, X_A) = (\sqrt{\Delta_v^2 + 8t^2} - \Delta_v)/2$ and extract $\Delta_v \simeq 140$ meV when reading $\Delta(X^o_A, X_A) \simeq 20$ meV from the experiments and assuming again that $t \simeq 40$ meV. With the above estimation, the band-edge structure of the 3L MoS_2 at the $K^{\pm}$ points of the Brillouin zone is concluded to consist of two conduction band subbands split by 50 meV and four valence band subbands with outer two subbands split by 180 meV and the inner two subbands split by 140 meV.

4. Conclusion

We have performed magneto-reflectance measurements along with $\mathbf{k}\cdot\mathbf{p}$ theory based modelling on few-layer MoS_2 encapsulated in hBN structures, revealing the intralayer and interlayer nature of the newly discovered transitions. Such resonances form due to the hybridization of valence and conduction bands states when one adds new layers to the system.

The experiment (i) displays the new excitonic resonances and their number in bi- and trilayers; (ii) demonstrates that *g*-factors of intralayer and interlayer excitons have opposite signs; (iii) the *g*-factor values of interlayer excitons are much larger (in magnitude) than those of intralayer ones.

The symmetry based $\mathbf{k}\cdot\mathbf{p}$ description of the bi- and trilayers provides a natural explanation for the aforementioned experimental observations. Moreover, from the general symmetry point of view the theoretical model also predicts (i) the renormalization of the band gap E_g and spin splittings Δ_c, Δ_v; (ii) the deviation of the bi- and trilayer exciton *g*-factors from their monolayer analogs. These two phenomena appear as a result of the coupling between different layers of the system and effects of dielectric screening induced by hBN.

Finally, we point out some unique properties of the exciton states of the trilayer. First, we mention the existence of two groups of exciton resonances—'even' and 'odd', which do not interact with each other because they belong to different irreps of the in-plane mirror symmetry of the system. However, electric field, applied perpendicularly to the crystal's plane, violates this symmetry and causes the controllable coupling of these states. Such feature can be used in future exciton based applications. We also note that the positive and negative electrical charges of interlayer excitons are separated between different layers. Such a property can be interesting in photovoltaic applications of S-TMD systems.

Acknowledgments

The work has been supported by the EC Graphene Flagship project (no. 785219), the ATOMOPTO project (TEAM programme of the Foundation for Polish Science co-financed by the EU within the ERDFund), the National Science Centre, Poland (grants no. DEC-2013/10/M/ST3/00791, UMO-2017/24/C/ST3/00119), the Nanofab facility of the Institut Neel, CNRS/UGA and the LNCMI-CNRS, a member of the European Magnetic Field Laboratory (EMFL). KW and TT acknowledge support from the Elemental Strategy Initiative conducted by the MEXT, Japan and and the CREST (JPMJCR15F3), JST.

Appendix A. Samples and experimental setups

In order to provide even and charged-defect-free support to van der Waals heterostructures studied in this work we assembled them on ultraflat unoxidized silicon (Si) substrates from Ted Pella Inc., whose surface roughness amounts to about one-tenth of that of standard Si/SiO_2 wafers. Each heterostructure consisted of three flakes obtained by means of mechanical exfoliation and successively stacked one on top of another using dry transfer techniques: a 60–70 nm thick bottom hBN flake, a central MoS_2 flake of 1 ML, 2 ML or 3 ML thickness, and a 10–15 nm thick top hBN flake.

The optimum thicknesses of hBN flakes were estimated on the basis of transfer-matrix simulations of RC spectra of complete heterostructures, aiming at maximizing the visibility of absorption resonances in MoS_2 flakes while keeping the thickness of bottom hBN flakes below 100 nm (a value up to which our exfoliation method yields a rich harvest of flat, defect-free flakes with large-area terraces of constant thickness).

Using high-purity ELP BT-150E-CM tape from Nitto Denko, bottom hBN flakes were exfoliated from high-quality bulk crystals grown under high-pressure conditions [41] and then transferred in a non-deterministic way onto clean and freshly annealed at 200 °C Si substrates. The MoS_2 flakes were obtained by means of two-stage, tape- and polydimethylsiloxane (PDMS)-based exfoliation of a bulk crystal purchased from HQ Graphene and then stacked on the bottom hBN flakes using an all-dry deterministic stamping technique [40]. The same procedure was applied also to the top hBN flakes. While performing deterministic transfers, special attention was paid to mutual angular alignment of the flakes and to immediate 10 min-long after-transfer annealing of the samples at 180 °C on a hot plate kept in clean ambient atmosphere.

Optical microscope images of investigated heterostructures which were fabricated in this way are shown in figures A1 (a)–(c). The spots of brown-to-blue colour visible in all images are up to 60 nm-high bubbles of air and/or water vapour (possibly with some amount of hydrocarbons) trapped between either the MoS_2 and the top hBN flake or the two hBN flakes. Their appearance directly results from the corrugation of thin, soft and flexible top hBN flakes supported by a PDMS stamp. Importantly, the areas between the bubbles, whose size reaches up to five by 10 μm, exhibit very flat and high-quality intefraces between the constitutent flakes, as revealed with optical measurements and atomic force microscopy (AFM) characterization.

An example of tapping-mode AFM imaging performed on finished heterostructures with the use of digital instruments dimension 3100 microscope is shown in figures A1(d)–(f). The false colour AFM images correspond to respective locations marked in panels (a)–(c) with orange circles. The grey arrows represent the line profiles drawn in figure A1(g) and labelled with the same numbers as in images (d)–(f). As can be seen, the profiles unambiguously confirm the mono-, bi-, and trilayer thickness of MoS_2 flakes incorporated into the heterostructures shown in the upper row of figure A1.

Compared to based on neutron scattering measurements estimation equal to 0.615 nm [46], the value of 0.79 nm we got for the monolayer most probably indicates that the equilibrium distance between the hBN and MoS_2 layers differs from that between two neighboring MoS_2 layers in a bulk crystal. A smaller single-layer step hight obtained for the second and third layer in the bi- and trilayer MoS_2 flakes, on the other hand, rather manifests the existence of more complex interaction picture between hBN and MoS_2 layers in corresponding heterostructures.

Measurements at zero magnetic field were carried out with the aid of a continuous flow cryostat mounted on $x-y$ motorized positioners. The samples were placed on a cold finger of the cryostat. The temperature of the samples was kept at 5 K. The excitation light was focused by means of a 50× long-working distance objective with a 0.5 numerical aperture producing a spot of about 1 μm. The signal was collected via the same microscope objective, sent through a 0.5 m monochromator, and then detected by a CCD camera.

Magneto-optical experiments were performed in the Faraday configuration using an optical-fiber-based insert placed in a resistive or a superconducting magnet producing magnetic fields up to 29 T or 14 T, respectively. The sample was mounted on top of an $x-y-z$ piezo-stage kept in gaseous helium at $T = 4.2$ K. The μ-RC experiments were performed with the use of 100 W tungsten halogen lamp. The excitation light was coupled to an optical fiber with a core of 50 μm diameter and focused on the sample by an aspheric lens (spot diameter around 10 μm). The signal was collected by the same lens, injected into a second optical fiber of the same diameter, and analyzed by a 0.5 m long monochromator equipped with a CCD camera. A combination of a quarter wave plate and a polarizer are used to analyse the circular polarization of signals.

Appendix B. Bilayer in magnetic field

The magnetic field correction to the valence band Hamiltonian at the K^+ point written in the basis $\{|\Psi_v^{(1)}\rangle \otimes |s\rangle, |\Psi_v^{(2)}\rangle \otimes |s\rangle\}$ is $\delta H_{vs}^{(2)} = \left(G_v^{(2)} + \sigma_s \mathcal{I}\right)\mu_B B$. Here μ_B is the Bohr magneton, B is the magnetic field, applied perpendicularly to the bilayer plane, $\mathcal{I}$ is the unit matrix and

$$G_v^{(2)} = \begin{bmatrix} g_v - \delta g_v & 0 \\ 0 & -g_v + \delta g_v \end{bmatrix}. \qquad \text{(B.1)}$$

The correction to the conduction band Hamiltonian written in the basis $\{|\Psi_c^{(1)}\rangle \otimes |s\rangle, |\Psi_c^{(2)}\rangle \otimes |s\rangle\}$ has the same form $\delta H_c^{(2)} = \left(G_c^{(2)} + \sigma_s \mathcal{I}\right)\mu_B B$, where

$$G_c^{(2)} = \begin{bmatrix} g_c - \delta g_c & 0 \\ 0 & -g_c + \delta g_c \end{bmatrix} \mu_B B. \qquad \text{(B.2)}$$

The expressions for g_v, g_c, δg_v, δg_c are derived in [28]. The corrections to the Hamiltonians provide the energy shifts of excitons in magnetic field. The intralayer X_A and X_B excitons, constructed from the quasiparticles at the K^+ point of bilayer, are active in $\sigma^\pm$ polarizations. The corresponding energy shifts are linear in magnetic field $\delta E_{A,B}^{\sigma^\pm} = \pm g_{A,B}^{(2)} \mu_B B$. The g-coefficients of such exciton transitions are

$$g_A^{(2)} = -g_u + (g_c - \delta g_c) - (g_v - \delta g_v)\frac{\Delta_v}{\sqrt{\Delta_v^2 + 4t^2}}, \qquad \text{(B.3}a\text{)}$$

$$g_B^{(2)} = g_u + (g_c - \delta g_c) - (g_v - \delta g_v)\frac{\Delta_v}{\sqrt{\Delta_v^2 + 4t^2}}. \qquad \text{(B.3}b\text{)}$$

We introduced $g_u = 2m_0 u^2/\hbar^2 \Delta_c$ parameter, which originates from k-dependent admixture of conduction bands. The mixing is negligibly small in the absence of magnetic field, but gives finite correction if $B \neq 0$. The interlayer excitons X'_A and X'_B at the bilayer K^+ point are also active in $\sigma^\pm$ polarizations with the magnetic shifts $\delta E_{A',B'}^{\sigma^\pm} = \pm g_{A',B'}^{(2)} \mu_B B$ respectively. The corresponding g-coefficients are

$$g_{A'}^{(2)} = g_u + (g_c - \delta g_c) + (g_v - \delta g_v)\frac{\Delta_v}{\sqrt{\Delta_v^2 + 4t^2}}, \qquad \text{(B.4}a\text{)}$$

$$g_{B'}^{(2)} = -g_u + (g_c - \delta g_c) + (g_v - \delta g_v)\frac{\Delta_v}{\sqrt{\Delta_v^2 + 4t^2}}. \qquad \text{(B.4}b\text{)}$$

Note that there are the following relations between g-coefficients of interlayer and intralayer exciton transitions

$$g_A^{(2)} + g_{A'}^{(2)} = g_B^{(2)} + g_{B'}^{(2)} = 2(g_c - \delta g_c), \qquad \text{(B.5}a\text{)}$$

$$g_{A'}^{(2)} - g_B^{(2)} = g_{B'}^{(2)} - g_A^{(2)} = (g_v - \delta g_v)\frac{2\Delta_v}{\sqrt{\Delta_v^2 + 4t^2}}, \qquad \text{(B.5}b\text{)}$$

$$g_B^{(2)} - g_A^{(2)} = g_{A'}^{(2)} - g_{B'}^{(2)} = 2g_u. \qquad \text{(B.5c)}$$

One can mention that the corresponding transitions at the K$^-$ point in $\sigma^\pm$ polarizations are characterized by the same values $\pm g_{A,B}^{(2)}$ and $\pm g_{A',B'}^{(2)}$ as in K$^+$ point. This is the consequences of time reversal and inversion symmetries of the crystal. As a result, we can restore the absorption spectra of the bilayer in σ^- and σ^+ polarizations using our methodology of the experiment—by measuring the reflected light in fixed σ^+ polarization and changing the orientation of magnetic field from B to $-B$. The change of the direction of the magnetic field to $-B$ in experiment mimics the transitions in σ^- polarization of the reflected light.

We use the formula $g = [E^{\sigma^+}(B) - E^{\sigma^+}(-B)]/\mu_B B = [\delta E^{\sigma^+}(B) - \delta E^{\sigma^+}(-B)]/\mu_B B$ for exciton's g-factor. As a result the intralayer and interlayer A, B excitons have $2g_{A,B}^{(2)}$ and $2g_{A',B'}^{(2)}$ g-factors, respectively.

The possible signs of intra- and interlayer exciton g-factors can be obtained from the expressions (B.3*a*), (B.3*b*), (B.4*a*) and (B.4*b*). Indeed, in the experiment we have $2g_{A,B}^{(2)} \approx -4$. It means that corrections g_u, δg_c and δg_v are not significally large, and therefore very roughly $2g_{A,B}^{(2)} \approx 2(g_c - g_v)$ is nothing but the g-factors of monolayer A and B excitons, for which we know that $g_v > g_c > 0$ [47]. Substituting the positive g_c and g_v into equations (B.4*a*) and (B.4*b*) one can see that $2g_{A',B'}^{(2)} > 0$, which is confirmed from the experiment.

Appendix C. Trilayer in magnetic field

The magnetic field correction to the valence and conduction band Hamiltonians written in the basis $\{|\Psi_n^{(1)}\rangle \otimes |s\rangle, |\Psi_n^{(2)}\rangle \otimes |s\rangle, |\Psi_n^{(3)}\rangle \otimes |s\rangle\}$, is $\delta H_{ns}^{(3)} = \left(G_n^{(3)} + \sigma_s \mathcal{I}\right)\mu_B B$ where

$$G_n^{(3)} = \begin{bmatrix} g_n - \delta g_n & 0 & \bar{g}_n \\ 0 & -g_n + 2\delta g_n & 0 \\ \bar{g}_n & 0 & g_n - \delta g_n \end{bmatrix}. \qquad \text{(C.1)}$$

Here $n = v, c$ and $\bar{g}_c$ and $\bar{g}_v$ are the additional parameters which describe the magnetic dependent coupling between layers of the system [28]. In new basis, defined in the main part of the text, the full Hamiltonians $H_{ns}^{(3)} + \delta H_{ns}^{(3)}$ are reduced to a block-diagonal form. Namely, the $G_n^{(3)}$ matrix transforms to

$$\mathcal{G}_n^{(3)} = \begin{bmatrix} g_n - \delta g_n + \bar{g}_n & 0 & 0 \\ 0 & -g_n + 2\delta g_n & 0 \\ 0 & 0 & g_n - \delta g_n - \bar{g}_n \end{bmatrix}. \qquad \text{(C.2)}$$

The 1×1 block corresponds to odd states $|\Upsilon_{ns}^{(3)}\rangle \otimes |s\rangle$ with total energies

$$E_{ns}^o(B) = E_n + \sigma_s \frac{\Delta_n}{2} + (g_n - \delta g_n - \bar{g}_n + \sigma_s)\mu_B B, \qquad \text{(C.3)}$$

with $E_v = 0$ and $E_c = E_g$. The expressions coincide with the monolayer ones, but with the new g-coefficient $g_n - \delta g_n + \bar{g}_n$. Moreover, the $uk_\pm$ terms do not affect the odd states, and therefore such excitons have the same reduced masses as their monolayer analogs. Hence the corresponding trilayer exciton line has the same optoelectronic properties as it's monolayer analog. The odd A and B exciton transitions at the K$^+$ point are active only in σ^+ polarization. The corresponding energy shift in magnetic field is $\delta E_{A^o,B^o}^{\sigma^+} = [(g_c - \delta g_c) - (g_v - \delta g_v) - \bar{g}_c + \bar{g}_v]\mu_B B$. The same type of transitions at the K$^-$ point are active in σ^- polarization and have the energy shift in magnetic field $\delta E_{A^o,B^o}^{\sigma^-} = -\delta E_{A^o,B^o}^{\sigma^+}$. It immediately gives us $g_{X_{A,B}^o} = 2(g_c - g_v) - 4\mathfrak{g}$ for X_A^o and X_B^o exciton g-factors both for K$^+$ and K$^-$ points of trilayer. Here we introduce the parameter

$$\mathfrak{g} = \frac{1}{2}\Big(\delta g_c + \bar{g}_c - \delta g_v - \bar{g}_v\Big). \qquad \text{(C.4)}$$

From the experiment we know that $g_{X_A^o} \approx -4.5$, which is close to monolayer $g_{X_A} = 2(g_c - g_v) \approx -4$. Therefore, we can roughly estimate $\mathfrak{g} \approx 0.125$.

The second block is 2×2 matrix, written in the basis of even states $\{|\Upsilon_n^{(1)}\rangle \otimes |s\rangle, |\Upsilon_n^{(2)}\rangle \otimes |s\rangle\}$. Note that the structure of this matrix does not coincide with the structure of $G_n^{(2)}$. Therefore the subsystem of even states of trilayer demonstrates another behavior in magnetic field than it's bilayer analog. The conduction band states in K$^+$ point are decoupled and have the energies

$$E_{cs}^{(1)} = E_g + \sigma_s \frac{\Delta_c}{2} + (g_c - \delta g_c + \bar{g}_c + \sigma_s - 2\sigma_s g_u)\mu_B B, \qquad \text{(C.5a)}$$

$$E_{cs}^{(2)} = E_g - \sigma_s \frac{\Delta_c}{2} - (g_c - 2\delta g_c - \sigma_s - 2\sigma_s g_u)\mu_B B. \qquad \text{(C.5b)}$$

The conduction band energies correspond to the states $\{|\Upsilon_c^{(1)}\rangle \otimes |s\rangle, |\Upsilon_c^{(2)}\rangle \otimes |s\rangle\}$. The valence band energies of admixed states as a function of magnetic field B are calculated similarly to the bilayer case.

The energy shifts of intralayer A and B excitons in $\sigma^\pm$ polarizations at the K$^+$ point are $\delta E_{A,B}^{\sigma^\pm} = [\pm g_{A,B}^{(3)} + \mathfrak{g}]\mu_B B$, where

$$g_A^{(3)} = -2g_u + \left(g_c - \frac{3}{2}\delta g_c + \frac{1}{2}\bar{g}_c\right) - \left(g_v - \frac{3}{2}\delta g_v + \frac{1}{2}\bar{g}_v\right)\frac{\Delta_v}{\sqrt{\Delta_v^2 + 8t^2}}, \qquad \text{(C.6a)}$$

$$g_B^{(3)} = 2g_u + \left(g_c - \frac{3}{2}\delta g_c + \frac{1}{2}\bar{g}_c\right) - \left(g_v - \frac{3}{2}\delta g_v + \frac{1}{2}\bar{g}_v\right)\frac{\Delta_v}{\sqrt{\Delta_v^2 + 8t^2}}. \qquad \text{(C.6b)}$$

The energy shifts for interlayer A' and B' excitons in both polarizations have the form $\delta E^{\sigma^\pm}_{A',B'} = [\pm g^{(3)}_{A',B'} + \mathfrak{g}]\mu_B B$, where

$$g^{(3)}_{A'} = 2g_u + \left(g_c - \frac{3}{2}\delta g_c + \frac{1}{2}\bar{g}_c\right) + \left(g_v - \frac{3}{2}\delta g_v + \frac{1}{2}\bar{g}_v\right)\frac{\Delta_v}{\sqrt{\Delta_v^2 + 8t^2}}, \qquad (C.7a)$$

$$g^{(3)}_{B'} = -2g_u + \left(g_c - \frac{3}{2}\delta g_c + \frac{1}{2}\bar{g}_c\right) + \left(g_v - \frac{3}{2}\delta g_v + \frac{1}{2}\bar{g}_v\right)\frac{\Delta_v}{\sqrt{\Delta_v^2 + 8t^2}}. \qquad (C.7b)$$

In the absence of $\mathfrak{g}$ the latter results coincide with the bilayer case up to redefinition of the parameters. The non-zero value of $\mathfrak{g}$ shows remarkable difference between pure bilayer and effective bilayer cases. The corresponding energy shifts in $\sigma^\pm$ polarizations at the K^- point are $\delta E^{\sigma^\pm}_{A,B} = [\pm g^{(3)}_{A,B} - \mathfrak{g}]\mu_B B$ and $\delta E^{\sigma^\pm}_{A',B'} = [\pm g^{(3)}_{A',B'} - \mathfrak{g}]\mu_B B$.

This non-equivalency makes the analysis of the g-factors of the system more complicated. Let us consider the results of the measurements presented on the figure 8 more carefully, focusing mainly on X_A and X'_A exciton transitions. Again, according to the methodology of our experiment we measure the g-factor using the formula $g = [\delta E^{\sigma^+}(B) - \delta E^{\sigma^+}(-B)]/\mu_B B$. Then the g-factors at the K^+ point of intralayer X_A, X_B and interlayer X'_A, X'_B excitons are $g^{K^+}_{X_{A,B}} = 2g^{(3)}_{A,B} + 2\mathfrak{g}$ and $g^{K^+}_{X_{A',B'}} = 2g^{(3)}_{A',B'} + 2\mathfrak{g}$ respectively. For K^- point transitions we obtain $g^{K^-}_{X_{A,B}} = 2g^{(3)}_{A,B} - 2\mathfrak{g}$ and $g^{K^-}_{X_{A',B'}} = 2g^{(3)}_{A',B'} - 2\mathfrak{g}$. Taking into account the relative smallness of $\mathfrak{g}$ and absence of the results for magnetic field B larger than 14 T we suppose that the double g-factor structure of X_A and X'_A resonances is indistinguishable. Instead of this, probably, we observe only their average values $g_{X_{A,B}} = 2g^{(3)}_{A,B}$ and $g_{X_{A',B'}} = 2g^{(3)}_{A',B'}$ respectively. One can mention that these average g-factors surprisingly coincide with the ones we can get from the standard formula $g = [E^{\sigma^+}(B) - E^{\sigma^-}(B)]/\mu_B B = [\delta E^{\sigma^+}(B) - \delta E^{\sigma^-}(B)]/\mu_B B$. The analysis of the signs of intra- and interlayer exciton g-factors can be done in the same way as in bilayer case.

ORCID iDs

A O Slobodeniuk https://orcid.org/0000-0001-5798-0431
M Koperski https://orcid.org/0000-0002-8301-914X
M R Molas https://orcid.org/0000-0002-5516-9415
C Faugeras https://orcid.org/0000-0002-9615-8739

References

[1] Novoselov K S, Jiang D, Schedin F, Booth T J, Khotkevich V V, Morozov S V and Geim A K 2005 *Proc. Natl Acad. Sci. USA* **102** 10451

[2] Wang Q H, Kourosh K Z, Kis A, Coleman J N and Strano M S 2012 *Nat. Nanotechnol.* **7** 699

[3] Koperski M, Molas M R, Arora A, Nogajewski K, Slobodeniuk A, Faugeras C and Potemski M 2017 *Nanophotonics* **6** 1289

[4] Wang G, Chernikov A, Glazov M M, Heinz T F, Marie X, Amand T and Urbaszek B 2018 *Rev. Mod. Phys.* **90** 21001

[5] Mak K F, Lee C, Hone J, Shan J and Heinz T F 2010 *Phys. Rev. Lett.* **105** 136805

[6] Splendiani A, Sun L, Zhang Y, Li T, Kim J, Chim C Y, Galli G and Wang F 2010 *Nano Lett.* **10** 1271

[7] Withers F *et al* 2015 *Nat. Mater.* **14** 301

[8] Withers F *et al* 2015 *Nano Lett.* **15** 8223

[9] Komsa H P and Krasheninnikov A V 2013 *Phys. Rev.* B **88** 085318

[10] Clark G, Schaibley J R, Ross J, Taniguchi T, Watanabe K, Hendrickson J R, Mou S, Yao W and Xu X 2016 *Nano Lett.* **16** 3944

[11] Schwarz S *te al* 2016 *2D Mater.* **3** 025038

[12] Shinde S M, Dhakal K P, Chen X, Yun W S, Lee J, Kim H and Ahn J H 2018 *NPG Asia Mater.* **10** 468

[13] Ruiz-Tijerina D A, Danovich M, Yelgel C, Zólyomi V and Fal'ko V I 2018 *Phys. Rev.* B **98** 035411

[14] Sun Y, Wang D and Shuai Z 2016 *J. Phys. Chem.* C **120** 21866

[15] Bradley A J *et al* 2015 *Nano Lett.* **15** 2594

[16] Fang S, Defo R K, Shirodkar S N, Lieu S, Tritsaris G A and Kaxiras E 2015 *Phys. Rev.* B **92** 205108

[17] Cheiwchanchamnangij T and Lambrecht W R L 2012 *Phys. Rev.* B **85** 205302

[18] Padilha J E, Peelaers H, Janotti A and van de Walle C G 2014 *Phys. Rev.* B **90** 205420

[19] Debbichi L, Eriksson O and Lebègue S 2014 *Phys. Rev.* B **89** 205311

[20] Arora A, Koperski M, Nogajewski K, Marcus J, Faugeras C and Potemski M 2015 *Nanoscale* **7** 10421

[21] Arora A, Nogajewski K, Molas M, Koperski M and Potemski M 2015 *Nanoscale* **7** 20769

[22] Molas M R, Nogajewski K, Slobodeniuk A O, Binder J, Bartos M and Potemski M 2017 *Nanoscale* **9** 13128

[23] Zeng H *et al* 2013 *Sci. Rep.* **3** 1608

[24] Zhang Y *et al* 2014 *Nat. Nanotechnol.* **9** 111

[25] Gong Z, Liu G B, Yu H, Cui X, Xu X and Yao W 2013 *Nat. Commun.* **4** 2053

[26] Kormányos A, Zólyomi V, Fal'ko V I and Burkard G 2018 *Phys. Rev.* B **98** 035408

[27] Bernardi M, Palummo M and Grossman J C 2013 *Nano Lett.* **13** 3664

[28] Arora A, Koperski M, Slobodeniuk A O, Nogajewski K, Schmidt R, Schneider R, Molas M R, Michaelis de Vasconcellos S, Bratschitsch R and Potemski M 2019 *2D Mater.* **6** 015010

[29] Horng J, Stroucken T, Zhang L, Paik E Y, Deng H and Koch S W 2018 *Phys. Rev.* B **97** 241404

[30] Arora A *et al* 2017 *Nat. Commun.* **8** 639

[31] Wierzbowski J *et al* 2017 *Sci. Rep.* **7** 12383

[32] Wang G *et al* 2017 *Phys. Rev. Lett.* **119** 047401

[33] Vaclavkova D, Wyzula J, Nogajewski K, Bartos M, Slobodeniuk A O, Faugeras C, Potemski M and Molas M R 2018 *Nanotechnology* **29** 325705

[34] Chen S Y, Goldstein T, Tong J, Taniguchi T, Watanabe K and Yan J 2018 *Phys. Rev. Lett.* **120** 046402
[35] Cadiz F *et al* 2017 *Phys. Rev.* X **7** 021026
[36] Pisoni R *et al* 2018 *Phys. Rev. Lett.* **121** 247701
[37] Kormányos A, Burkard G, Gmitra M, Fabian J, Zólyomi V, Drummond N D and Fal'ko V 2015 *2D Mater.* **2** 022001
[38] Liu G B, Xiao D, Yao Y, Xu X and Yao W 2015 *Chem. Soc. Rev.* **44** 2643
[39] Terrones H, López-Urías F and Terrones M 2013 *Sci. Rep.* **3** 1549
[40] Castellanos-Gomez A, Buscema M, Molenaar R, Singh V, Janssen L, van der Zant H S J and Steele G A 2014 *2D Mater.* **1** 011002
[41] Taniguchi T and Watanabe K 2007 *J. Cryst. Growth* **303** 525
[42] Koperski M, Molas M R, Arora A, Nogajewski K, Bartos M, Vaclavkova D, Wyzula J and Potemski M 2019 *2D Mater.* **6** 015001
[43] Mitioglu A A, Galkowski K, Surrente A, Klopotowski L, Dumcenco D, Kis A, Maude D K and Plochocka P 2016 *Phys. Rev.* B **93** 165412
[44] Stier A V, McCreary K M, Jonker B T, Kono J and Crooker S A 2016 *Nat. Commun.* **7** 10643
[45] Wu Y J, Shen C, Tan Q H, Shi J, Liu X F, Wu Z H, Zhang J, Tan P H and Zheng H Z 2018 *Appl. Phys. Lett.* **112** 153105
[46] Wakabayashi N, Smith H G and Nicklow R M 1975 *Phys. Rev.* B **12** 659
[47] Kormányos A, Zólyomi V, Drummond N D and Burkard G 2014 *Phys. Rev.* X **4** 011034